RSC Sustainability

ROYAL SOCIETY OF CHEMISTRY

PAPER

View Article Online
View Journal | View Issue

Check for updates

Cite this: *RSC Sustainability*, 2025, **3**, 3530

Facile fabrication of magnetite (Fe_3O_4) nanoparticles by hydrothermal carbonization of waste iron supplements†

Ahmed I. Yunus, [a] Samuel A. Darko,*[bc] Yongsheng Chen [a] and Joe F. Bozeman III*[ad]

We report a novel, time-dependent synthesis of magnetic magnetite (Fe_3O_4) and maghemite (Fe_2O_3) nanoparticles (MNPs) embedded in hydrochar *via* hydrothermal carbonization (HTC) of expired pharmaceutical waste containing iron-based supplements. This unique circular reuse and waste valorization proposition offers pharmaceutical waste as a sustainable iron-rich feedstock for MNP fabrication. The synthesis was conducted at a fixed temperature of 275 °C with residence times of 6 and 12 h, producing maghemite- and magnetite-dominant phases, respectively. Unlike conventional methods that rely on high temperatures, toxic reagents, or complex protocols, our approach offers a low-cost, sustainable route for functional nanomaterial production. The structural, morphological, and surface chemical characteristics of the MNP hydrochar were elucidated using XRD, SEM, and FTIR analyses. To evaluate environmental sustainability, we performed a comparative life cycle assessment (LCA) against co-precipitation and pyrolysis/gasification methods. The HTC route exhibited the lowest environmental impact across multiple TRACI 2.1 impact categories. Finally, the adsorption performance of the fabricated MNP hydrochar was assessed in a model methylene blue (MB) wastewater system, demonstrating >95% removal efficiency and an adsorption capacity of 1.38 mg g^{-1}. These findings present a viable pathway for integrating waste valorization, green nanomaterial synthesis, and sustainable wastewater treatment.

Received 30th April 2025
Accepted 17th June 2025

DOI: 10.1039/d5su00312a

rsc.li/rscsus

Open Access Article. Published on 18 junio 2025. Downloaded on 30/01/2026 01:29:39 p. m..
This article is licensed under a Creative Commons Attribution-NonCommercial 3.0 Unported Licence.

Sustainability spotlight

With the increasing demand for nanomaterials, sustainable fabrication methods are urgently needed. This study introduces a low-energy hydrothermal carbonization (HTC) route to synthesize magnetite and maghemite nanoparticles (MNPs) from expired iron-rich pharmaceutical waste. Through integrated life cycle assessment (LCA), we demonstrate substantially lower environmental impacts compared to conventional co-precipitation and pyrolysis/gasification processes. The fabricated MNPs effectively removed methylene blue (MB) dye from simulated wastewater, illustrating how nanoscale materials can drive macroscale environmental benefits. By coupling waste valorization, green nanomaterial synthesis, environmental impact assessment, and functional validation, this work advances circular economy strategies for sustainable chemical manufacturing. It directly contributes to the UN Sustainable Development Goals (SDGs) of responsible consumption and production; industry, innovation, and infrastructure; clean water and sanitation; climate action.

1 Introduction

The paradigm shift from the industrial age to the digital and electronic age, encompassing artificial intelligence and machine learning landscape, puts pressure on sustaining natural resources globally. These natural resources include metals for nano-materials, which are highly used for producing microchips, semiconductors, and other digital hardware components.[1–3] Consequentially, nanoparticles are being fabricated at an astonishing pace to enhance the miniaturization of digital hardware. Iron (Fe)-doped carbon—the nanoparticles of focus in the present study—is essential to this new global economy.[4–6] At the same time, metal waste generation—from extraction to the end of life of metal-based products—has led to

[a]*School of Civil and Environmental Engineering, Georgia Institute of Technology, Atlanta, GA 30318, USA. E-mail: sdarko@stu.edu; joe.bozeman@ce.gatech.edu; ayunus7@gatech.edu; yongsheng.chen@ce.gatech.edu*

[b]*Department of Physics and Engineering, Benedict College, Columbia, SC 29204, USA*

[c]*College of Science and Technology, St. Thomas University, Miami Gardens, FL 33054, USA*

[d]*School of Public Policy, Georgia Institute of Technology, Atlanta, GA 30332, USA*

† Electronic supplementary information (ESI) available: Section 1. FTIR, XRD, SEM, and EDX characterization of solid MNP hydrochar. Section 2. LCA functional unit, scenarios, and study boundary. Section 3. LCA inventory, environmental impact assessment, and interpretation. Section 4. Comparative analysis of the ten (10) TRACI 2.1 impact categories. See DOI: https://doi.org/10.1039/d5su00312a

© 2025 The Author(s). Published by the Royal Society of Chemistry

Open Access Article. Published on 18 junio 2025. Downloaded on 30/01/2026 01:29:39 p. m..
This article is licensed under a Creative Commons Attribution-NonCommercial 3.0 Unported Licence.

a global waste management catastrophe. Therefore, new reuse avenues of metal waste, such as Fe, are urgently needed.

Fe, Fe-doped, or Fe-encapsulated carbons have become very attractive nanomaterials for hardware manufacturing to support the digital and electronic age. Due to Fe-doped carbons' superparamagnetic properties, their applications as nanoparticles are diverse and of utmost importance to the present study, wastewater treatment.[4–10] In wastewater treatment, disinfection and color, oil, and heavy metal removal are the main applications of Fe nanoparticles.[11–15] For example, previous studies have utilized Fe-doped carbon materials—such as biochar—for adsorption of oil and synthetic dyes (*e.g.*, methylene blue (MB)).[16–19] Other previous studies have used Fe nanoparticles—such as magnetite (Fe_3O_4)—for Fenton oxidation due to their ability to break down bacteria and organic pollutants through hydroxyl radical production.[12,20–22]

As a result of economic and environmental importance of Fe-doped nanoparticles, the synthesis of magnetic magnetite (Fe_3O_4) or maghemite (Fe_2O_3) nanoparticles (MNPs) has been the subject of many previous studies, with some even claiming their approach as "green" or sustainable.[4,6,11,16,17] However, a critical knowledge gap remains: these studies lack a comprehensive life cycle assessment (LCA) of their MNP fabrication process to quantify the environmental impact. Green or sustainable chemistry emphasizes reducing or eliminating the use and generation of hazardous chemicals in its processes.[23] The goal is to be safer, efficient, and environmentally friendly while eliminating waste.[24] For example, several studies have suggested that employing physical and chemical methods—such as ball milling, pyrolysis, co-precipitation, the sol–gel process, and electrochemical synthesis—are sustainable approaches.[7,25–31] However, these previous studies applied methods utilizing several reagents, and their fabrication steps were proven expensive and chemically intensive, and therefore were environmentally dangerous.[6,7,26,29,32]

A potential solution to reduce the expensive reagent use and hazardous fabrication activities associated with synthesizing and fabricating MNPs could be hydrothermal carbonization (HTC).[30,33,34] HTC is an effective technology for the treatment and conversion of diverse feedstocks—such as food waste, municipal waste, and plant material, to obtain energy-dense biocrude, hydrochar, and other innocuous end products—which can be used as adsorbents in wastewater treatment and electronic component manufacturing among many others.[24,35–39]

To address the LCA-based critical knowledge gap in the evaluation of MNP fabrication, we examined the HTC process because the energy balance involved is quite interesting. Attractively, HTC feedstock does not need to be dried, allowing for large energy savings.[35] Also, a significant percentage of carbon in the original HTC feedstock remains integrated within the hydrochar (the HTC end-product), ultimately minimizing greenhouse gas emissions.[36,39] Lastly, HTC requires less material processing (*e.g.*, dewatering, sieving, grinding, *etc.*) and handling (*e.g.*, sterilization, dust removal, *etc.*).[34,37]

Building on these findings, our main goal is to fabricate MNPs using HTC with dietary Fe supplements as our rich source of Fe. This stems from the fact that, to sustainably fabricate MNPs, the incoming feedstock type is essential to ensure that the fabricated MNPs have the correct composition of crystallinity, nanoparticle sizes, and magnetic properties.[29,30,34,38] As a result, Fe-rich waste materials have been evaluated as sustainable feedstock with the potential to yield MNPs.[29,30,34,38] Examples of waste feedstocks with a high Fe content are steel slag, bauxite residue, Fe ore tailings, and spent catalysts from industrial reactors—such as hydrodesulfurization or Fischer–Tropsch.[40,41] These types of Fe-rich waste materials can ensure a greater yield of MNPs.[29,30,34,38]

To achieve our main goal of fabricating MNPs through the HTC route and comparatively evaluate this facile process with common processes, we established five (5) objectives. Our study follows the logical outline of these objectives, and they are (1) investigate the potential of HTC treatment in converting Fe-rich feedstock (*i.e.*, Fe dietary supplements) to MNPs by producing MNP hydrochar; (2) study the effect of temperature and reaction time on the yield and characteristics of the produced MNP hydrochar; (3) examine the microstructure and chemical composition of the produced MNP hydrochar using Fourier Transform Infrared (FTIR) spectroscopy, X-ray Diffraction (XRD), Scanning Electron Microscopy (SEM) and Energy Dispersive X-ray Spectroscopy (EDX); (4) investigate in a novel way the sustainability of HTC for MNP fabrication compared to pyrolysis/gasification and co-precipitation through a complete LCA; finally, (5) comparatively evaluate the adsorption performance of the HTC-fabricated MNP hydrochar in the removal of MB from wastewater.

2 Materials and methods

2.1 Raw materials

The feedstock used in the present study comprised over-the-counter expired Fe dietary supplements that a local healthcare facility donated. They contained ferrous fumarate (>95%) as the main ingredient along with others (<5%) (*i.e.*, amino acids, chelates, citrates, rice flour, and gelatin). Our HTC feedstock presents a sustainable pathway to reducing pharmaceutical waste. The target feedstock of this study was Fe-rich waste materials with 33–40% elemental Fe; hence, the availability of a large amount of expired Fe dietary supplements met this criterion. The Fe dietary supplements were in a capsule form, which was then opened to obtain the powdered Fe supplement, increasing its surface area and heterogeneity. The Fe supplement was also dry, requiring the addition of water for the HTC process.

2.2 Batch MNP hydrochar production

To satisfy objective 1, batch production of MNP hydrochar was conducted in a laboratory. All batch carbonization experiments were conducted following previously established procedures in the studies of Sarrion *et al.* (2023) and Berge *et al.* (2011).[42,43] The method used in the present study is illustrated in Fig. 1. Consequently, 20 g of feedstock and 20 g of deionized (DI) water were placed in 160 mL stainless steel tubular reactors (*i.e.*,

Open Access Article. Published on 18 junio 2025. Downloaded on 30/01/2026 01:29:39 p. m..
This article is licensed under a Creative Commons Attribution-NonCommercial 3.0 Unported Licence.

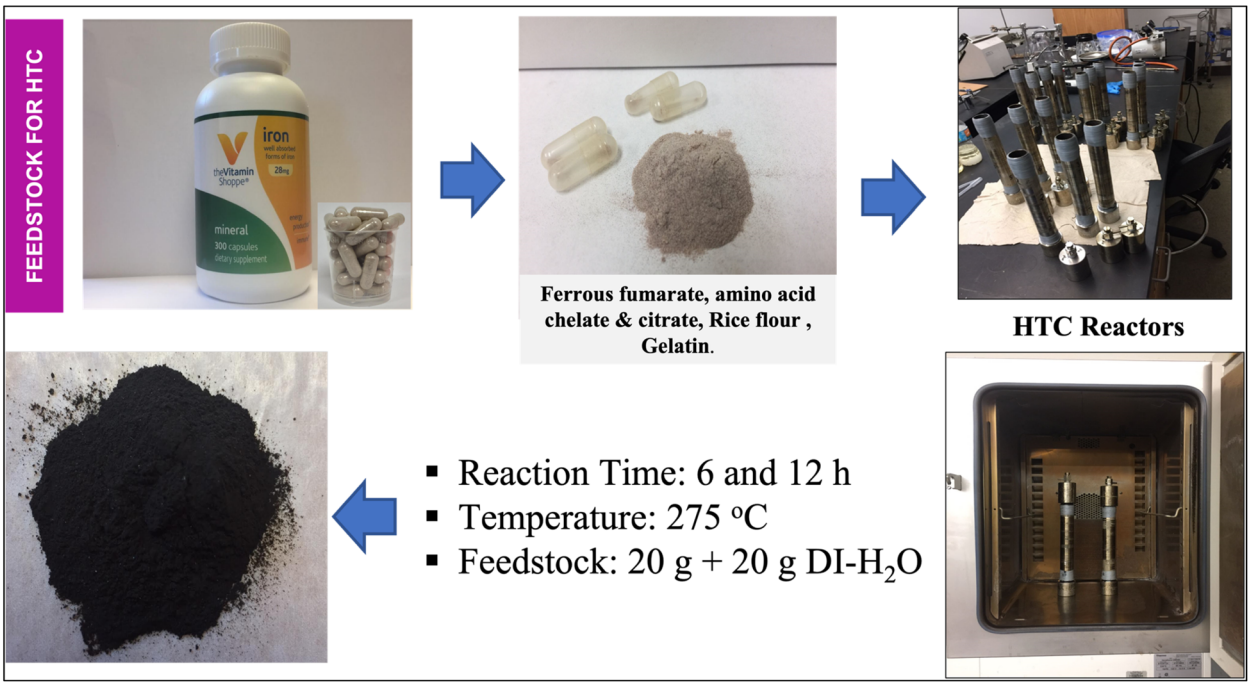

Fig. 1 Feedstock content and MNP hydrochar batch production method using HTC.

25.4 cm long) fitted with gas-sampling valves. All reactors in experimental triplicates were subsequently sealed and heated in a laboratory oven to the desired temperature of 275 °C for 6 and 12 hours (h) of reaction times, as illustrated in Fig. 1.

2.3 Phase quantification of MNP hydrochar

Quantification of the phases of the produced MNP hydrochar was conducted in steps to achieve objective 2. Firstly, after each batch production, when the reaction time was reached, the reactors were safely removed from the oven and placed in open air until they reached room temperature (~23 °C). The cooling stage took approximately three (3) h, which was not included in the total reaction time.

Secondly, after cooling, the gaseous product was discharged into a fume hood, and the solid phase was separated from the liquid by vacuum filtration. Then, the solid phase material was dried at 80 °C to remove residual moisture. MNP hydrochar is denoted using the following nomenclature: Fe(t), where Fe stands for the Fe supplement and t for the reaction time.

Lastly, a mass balance analysis of the HTC process was performed using the steps and equations in Sections 2.3.1 and 2.3.2. The inputs of the mass balance analysis were the DI water and feedstock, whereas the outputs were the solid phase (*i.e.*, dried MNP hydrochar), the liquid phase (process liquid or tar), and the gas phase. To quantitatively account for the gas phase, we assumed the difference between the initial and final masses of the solid and liquid phases.

2.3.1 Liquid phase content after HTC batch production. Since objective 2 focuses on the yield and characteristics, the liquid phase content of the produced MNP hydrochar was calculated using eqn (1) below:

$$\text{Moisture content} = \left(\frac{W_i - W_{OD}}{W_{OD}}\right) \times 100\% \quad (1)$$

Eqn (1) presents the formula for calculating the moisture content for MNP hydrochar, where W_i is the initial weight (feedstock) and W_{OD} (MNP hydrochar) is the weight after oven drying.

2.3.2 Solid phase content after HTC batch production. Next, in objective 2, the solid phase content was the focus of the HTC batch production process. The higher the solid phase yield, the higher the production of MNP hydrochar. Hence, the yield percentage of the MNP hydrochar at different reaction times was calculated using the following equation:

$$\text{MNP hydrochar yield} = \left(\frac{W_h}{W_f}\right) \times 100\% \quad (2)$$

Eqn (2) presents the solid phase yield % of HTC, where W_h is the weight of the dry MNP hydrochar product and W_f is the weight of the feedstock sample before HTC processing.

2.4 Characterization of the solid MNP hydrochar

To fulfill objective 3, the MNP hydrochar was characterized using FTIR, XRD, SEM, and EDX to elucidate its functional groups, crystalline structure, surface morphology, and elemental composition. The instrumentation and analytical rigor steps employed in this pursuit are detailed in Section 1 of the ESI.†

2.5 Life cycle assessment of MNP hydrochar production

Although numerous studies have labeled their MNP fabrication method as "green" or "sustainable," they lack adequate

© 2025 The Author(s). Published by the Royal Society of Chemistry

Open Access Article. Published on 18 junio 2025. Downloaded on 30/01/2026 01:29:39 p. m..
This article is licensed under a Creative Commons Attribution-NonCommercial 3.0 Unported Licence.

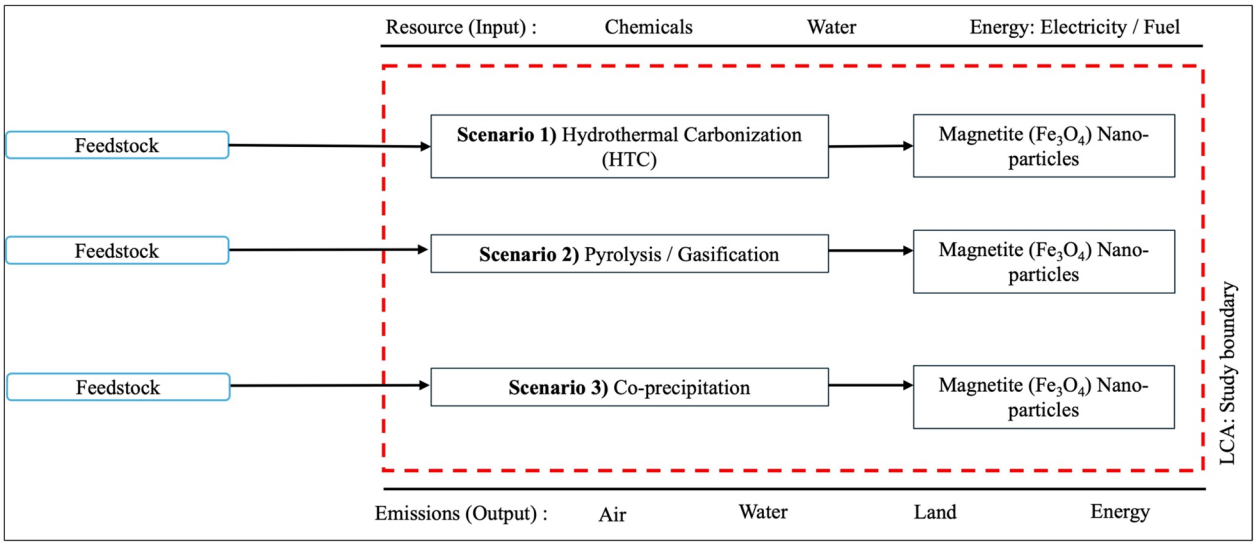

Fig. 2 System boundary for the LCA of magnetite (Fe_3O_4) nanoparticle (MNP) production *via* three pathways: (1) hydrothermal carbonization (HTC), (2) pyrolysis/gasification, and (3) co-precipitation. The red dashed box delineates the LCA study boundary, encompassing resource inputs (chemicals, water, and energy) and emissions outputs (air, water, land, and energy). Blue-outlined rectangles represent the feedstock input streams for each scenario.

quantitative evidence to substantiate these claims. In alignment with objective 4, the sustainability performance of HTC for MNP fabrication was systematically investigated and benchmarked against pyrolysis/gasification and co-precipitation. To ensure our method is reproducible and scientifically rigorous, we utilized the International Organization for Standardization (ISO) 14044:2006 framework for LCA, which provides a rigorous and internationally accepted methodology for evaluating environmental impacts across a process or system. Our comprehensive LCA approach is illustrated in Fig. 2 and summarized in Table 1.

Table 1 LCA of MNPs produced per gram of Fe-rich feedstock processed: resource (input) and emission (output) inventory data[a]

Parameter	Scenario 1: hydrothermal carbonization (HTC)[b]	Scenario 2: pyrolysis & gasification[c]	Scenario 3: co-precipitation[d]
Feedstock/chemicals			
Waste feedstock (g)	1 (Fe-rich waste feedstock)	1 (biomass waste feedstock)	N/A
Air input (L)	N/A	5	N/A
Water (mL)	1	N/A	N/A
$FeCl_3 \cdot 6H_2O$ (g)	N/A	0.7117	1.082
$FeSO_4 \cdot 7H_2O$ (g)	N/A	0.400	0.556
NH_4OH (mL)	N/A	60	20 (1 M)
NaOH (mL)	N/A	N/A	20
HCl (mL)	N/A	N/A	20 (5.49 mol L^{-1} solution)
Energy			
Heat energy (kW h)	0.32–0.35	0.33–0.93	0.07–0.09
Electricity (kW h)	0.80–0.85	0.81–1.85	0.37–0.41
Byproducts	MNP hydrochar, tar, and syngas	MNP biochar, tar, and syngas	MNPs and salt residue
Solid residue (g)	0.21–0.23	0.25–0.45	0.75–0.9
Tar byproduct (liquid) (g)	0.65–0.66	0.4–0.45	0.15–0.25
Syngas byproduct (gas) (g)	0.07–0.12	0–0.2	0
Reaction conditions			
Reaction temperature (°C)	275–300	280–800	60–80
Reaction atmosphere	Sealed autoclave or pressurized reactors (23 MPa (megapascals) to 40 MPa) and aqueous	Air and inert gas (N_2)	Aqueous and stirred
Reaction time (h)	6 to 12	1 to 3	0.5 to 2

[a] N/A = not typically applicable in the reaction process. [b] LCA inventory data for HTC were gathered from this study. [c] LCA inventory data for pyrolysis/gasification MNP fabrication method were from ref. 17, 29, 41, 44 and 45. [d] LCA inventory data for co-precipitation MNP fabrication method were from ref. 4, 6, 7, 11, 18, 19 and 46–48.

© 2025 The Author(s). Published by the Royal Society of Chemistry

Open Access Article. Published on 18 junio 2025. Downloaded on 30/01/2026 01:29:39 p. m..
This article is licensed under a Creative Commons Attribution-NonCommercial 3.0 Unported Licence.

Fig. 2 illustrates the study boundary for LCA evaluation between the three (3) scenarios (*i.e.*, HTC, pyrolysis/gasification, and co-precipitation), whereas Table 1 presents resource input and output inventory data. The functional unit is the total mass of MNPs produced per gram of Fe-rich feedstock processed. This functional unit is derived from the solid, liquid, and gas phase quantification (*i.e.*, mass balance analysis) of the HTC process used in this study (refer to Table 1). For comparative analysis with pyrolysis/gasification and co-precipitation processes, the mass yields of MNPs from literature studies were utilized, as presented in Table 1. This comparative LCA evaluation integrated process inventories, impact assessment, and multi-criteria ranking to elucidate the relative environmental implications of each fabrication route. Further in-depth methodological details on the functional unit, scenarios, and study boundary are outlined in Section 2 of the ESI.† More details on the LCA inventory, environmental impact assessment, and interpretation are also thoroughly presented in Section 3 of the ESI.†

2.6 Adsorption mechanism and kinetics of MNP hydrochar

Building on earlier results on the sustainability assessment of HTC as an alternative production pathway for MNPs, objective 5 was addressed by evaluating the synthetic color adsorption performance of HTC fabricated MNP hydrochar. The adsorption kinetic behavior and mechanism of the HTC fabricated MNP hydrochar is reported, offering insights into its real-world functional application for wastewater treatment.

To complete this last objective, single-use batch adsorption experiments were conducted to evaluate the removal efficiency of MB under isothermal conditions using the synthesized MNP hydrochar. The experiments were performed in 250 mL Erlenmeyer flasks containing 100 mL of MB solution at initial concentrations (C_O) of 5 mg L^{-1} and 10 mg L^{-1}. The adsorbent dosage was maintained at 1 g per 100 mL solution. The mixtures were then stirred at 150 rpm using a mechanical shaker at room temperature (23 °C). The adsorption process was 90 minutes, after which the samples were filtered to separate the adsorbent. The residual MB concentration in the supernatant was measured using a HACH DR 5000 ultraviolet-visible (UV-vis) spectrophotometer at a wavelength (λ) of 665 nm. All experiments were performed in triplicate, and the average values were reported to ensure accuracy and reproducibility. The percentage removal of MB was calculated using eqn (3).

$$\text{MB removal efficiency} = \left(\frac{C_O - C_f}{C_O}\right) \times 100\% \quad (3)$$

Eqn (3) presents the formula for removal efficiency calculation of MB using MNP hydrochar, where C_O and C_f represent the initial and equilibrium MB concentrations, respectively.

3 Results and discussion

3.1 Mass balance and MNP hydrochar yield

Phase quantification of MNP hydrochar was conducted with a simple mass balance analysis approach. The obtained results for MNP hydrochar under different HTC conditions are presented in Table 2. The table presents the average mass in and out, along with the standard error values, of the reactors after HTC. The reported values include the mass of MNPs hydrochar recovered, the liquid, and the gas from the triplicate experiments conducted at a constant temperature of 275 °C and with different reaction times (*i.e.*, 6 h and 12 h). In summary, the results indicate that the MNP hydrochar production decreases when reaction times increase (*i.e.*, from 6 h to 12 h), with the MNP hydrochar production as low as 8.2 g for Fe_{12h}. We posit that this low production is due to a large overall decomposition of the feedstock material or because the carbon in the feedstock progressively reacted and diffused out over time into the liquid and gas phases. This observation is contextualized in the subsequent paragraphs, where the evolution of carbon into the liquid, gas, and solid phase byproducts is discussed in greater detail.

The liquid phase byproduct reported in Table 2 includes three (3) different liquids: liquids collected by vacuum filtration after the HTC experiments, residual liquids evaporated while drying the MNP hydrochar in the oven, and liquid soaked by the filter paper. The first step of the HTC reaction is hydrolysis, which requires water to react with the feedstock to break bonds and enable the formation of new ones.[42,43] This hydrolysis step is inherently sensitive to the reaction conditions, such as temperature and time, which is crucial for determining the nature of the products formed.[42,43,49] Furthermore, understanding the effect of time is particularly important, as it governs not only the decomposition but also the yield and composition of the HTC process liquid and gas phases. The effect of time and temperature on the production of the HTC

Table 2 HTC mass balance and MNP hydrochar percent (%) yield of feedstock at 275 °C and two different reaction times

		Mass in	Mass out	Yield	Mass out	Yield	Mass out	Yield
Feedstock	Time (h)	Fe feedstock + water (1 : 1) (g)	MNP hydrochar (g)	Percentage (%)	Net liquid (g)	Percentage (%)	Gas[a] (g)	Percentage (%)
Iron supplement (Fe)	6	40.0 ± 0.0	8.95 ± 0.81	22.4	25.96 ± 0.62	64.9	2.74 ± 0.34	6.9
	12	40.0 ± 0.0	8.20 ± 0.81	20.5	26.39 ± 1.23	66.0	4.70 ± 0.34	11.8

[a] Gas weights were not measured but calculated by subtracting the initial and final masses of the solid and liquid phases.

© 2025 The Author(s). Published by the Royal Society of Chemistry

Open Access Article. Published on 18 junio 2025. Downloaded on 30/01/2026 01:29:39 p. m..
This article is licensed under a Creative Commons Attribution-NonCommercial 3.0 Unported Licence.

process liquid is evident in this present study as the net liquid increased (*i.e.*, 65–66%) with reaction time.

The gas phase generated after the HTC process presented noteworthy characteristics. Upon depressurization and venting of the reactors, a distinct pungent odor—reminiscent of sulfur-containing compounds (*e.g.*, hydrogen sulfide, H_2S)—was observed, suggesting the formation of volatile sulfurous species during feedstock decomposition.[50] Similar observation and evaluation were detailed by Wang *et al.* (2020) on HTC hydrochar fabrication.[50] By calculating the gas phase, it was observed that it increased as the HTC reaction time increased. From Table 2, it can be observed that the mass of the gas produced at Fe_{12h} (11.75%) is approximately two (2) times greater than the amount of gas produced at Fe_{6h} (6.85%). A similar trend is observed in the findings of relevant previous studies.[30,42] Hydrolysis and dehydration of the feedstock likely produced hydrogen sulfide (H_2S), sulfur dioxide (SO_2), and carbon dioxide (CO_2) as the dominant constituents of the gaseous phase.

The yield of MNP hydrochar is an important indicator of process efficiency and resource recovery; hence, the solid phase is most important to this present study. Table 2 additionally describes the solid phase yield of the MNP hydrochar of the HTC temperature (*i.e.*, 275 °C) and two (2) reaction times (*i.e.*, 6 and 12 h). The solid phase MNP hydrochar production decreased with an increase in reaction time. As shown in Table 2, 20.5–22.4% of the initial feedstock was retained as the MNP hydrochar. This solid yield falls within a favorable range for HTC systems and supports the material recovery goals outlined in objectives 1 and 2.

Notably, the MNP hydrochar yield showed a declining trend as the reaction time doubled, a behavior attributed to progressive decomposition and pyrolysis reactions. This decrease is closely connected with deoxygenation reactions and volatile matter conversion, as oxygen and hydrogen contents become lower at higher temperatures.[43] This shift in reactions also coincides with the formation of two (2) structurally related iron oxide phases—magnetite (Fe_3O_4) and maghemite (Fe_2O_3)—which collectively influence the functional performance and physicochemical properties of the fabricated MNP hydrochar.

3.2 Physico-chemical characteristics of the MNP hydrochar

3.2.1 FTIR spectra of MNP hydrochar. To understand the functional performance in the MNP hydrochar after HTC at different reaction times, FTIR spectroscopy was performed for the feedstock along with all MNP hydrochar samples. This ensures satisfying objective 3. From Fig. 3A, the peak observed at 3000 cm^{-1} in the feedstock indicates the presence of the –CH_3 stretch (methyl). This group disappears as the Fe-rich feedstock is being carbonized for 6 and 12 h reaction times. The loss of functional groups is due to the diverse thermal decomposition upon Fe synthesis.[29,34,41,48] A clear shift in the spectrum is observed when moving from the feedstock to the MNP hydrochar as the intensity of all the functional groups, bands, and peaks (% transmittance) decreases (Fig. 3A). Further explanation of the occurrence and disappearance of the illustrated functional groups in the FTIR plot is provided next.

The FTIR spectra of the feedstock and MNP hydrochar obtained at 6 and 12 h show absorbance peaks at 3400 cm^{-1} and

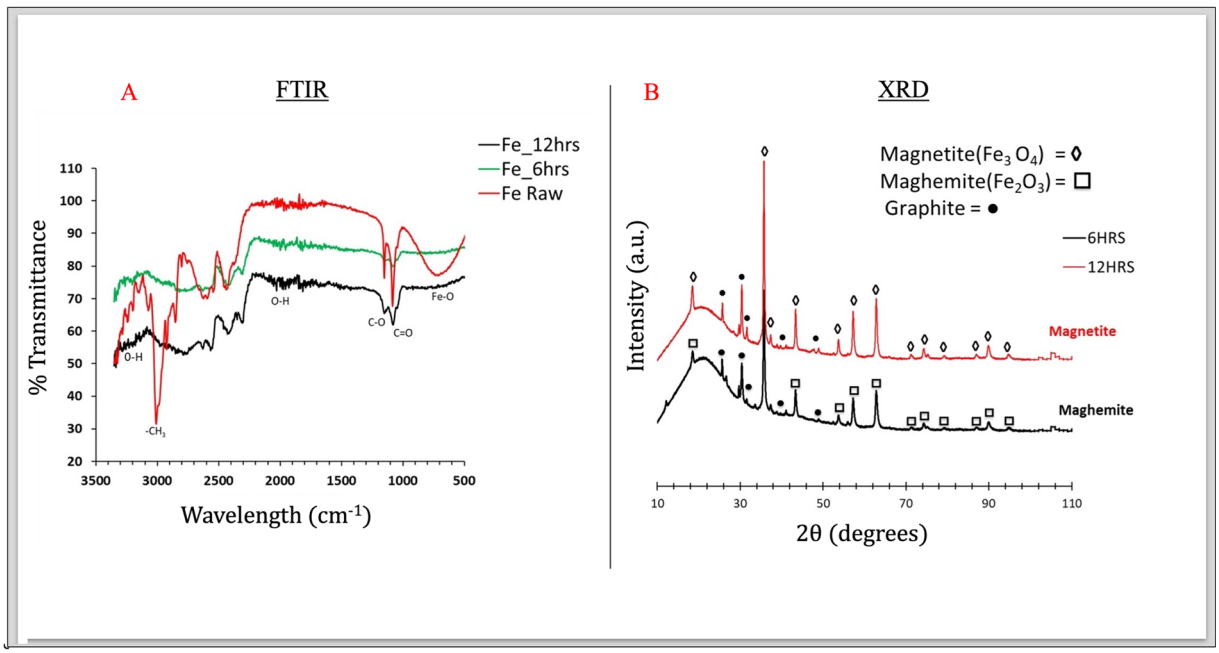

Fig. 3 (A and B) FTIR and XRD spectra of the raw Fe-rich feedstock and MNP hydrochar products at HTC times of 6 h and 12 h. In the FTIR plot, the raw feedstock spectrum is indicated in red and spectra of MNP hydrochar fabricated at 6 and 12 h are indicated in green and black, respectively. In the XRD plot, patterns of MNP hydrochar fabricated at 6 and 12 h are indicated in black and red. The XRD diffraction patterns show the phase identification of magnetite (Fe_3O_4) (◇), maghemite (Fe_2O_3) (□), and graphite (●) in the synthesized MNP hydrochar.

Open Access Article. Published on 18 junio 2025. Downloaded on 30/01/2026 01:29:39 p. m..
This article is licensed under a Creative Commons Attribution-NonCommercial 3.0 Unported Licence.

2000 cm^{-1} (Fig. 3A). We posit that these absorbance peaks are due to the O–H stretching vibration, which can be related to that of water in the sample. For the feedstock, the peak at 1100 cm^{-1} is due to the C=O stretching vibrations of the carbonyls (aldehyde, ketones esters, and carboxylic acids). However, in the MNP hydrochar carbonized for 6 and 12 h, these peaks are less prominent due to dehydration and decarboxylation, which eliminate oxygen-containing functional groups. Another feature of the raw feedstock is the presence of (Fe–O) at the wavenumber of 700 cm^{-1}, which indicates the presence of Fe bonded with oxygen in the material. After HTC for 6 and 12 h, the peaks (% transmittance) are reduced on the FTIR graph of the MNP hydrochar due to the oxidation process of HTC. This observation is critical, as it illustrates the phase transformation of Fe–O species into the desired magnetite (Fe_3O_4) and maghemite (Fe_2O_3) nanoparticles.

3.2.2 XRD spectra of MNP hydrochar. To further validate the phase transformation of the feedstock Fe–O species identified in the FTIR spectra (Fig. 3A), XRD analysis was conducted to confirm the crystalline structure and mineral phases present in the MNP hydrochar. The XRD intensity pattern highlighted in Fig. 3B represents the physical mineral components and crystal structures of the MNP hydrochar at 6 and 12 h reaction times. The MATCH 3 database—by "Crystal Impact"—search results showed intensity patterns that largely matched magnetite (Fe_3O_4), maghemite (Fe_2O_3), and some peaks corresponding to graphite. The results suggest that the minor graphite peak is a derivative of the carbonization of the organic material (*i.e.*, feedstock precursor material) added to Fe supplements—such as rice. Next, we discuss in detail the evaluation of the XRD intensity peaks to provide definitive evidence of the formation of magnetite (Fe_3O_4) and maghemite (Fe_2O_3) as required in objective 3.

As shown in Fig. 3B, the XRD technique determined that the fabricated MNP hydrochar exhibits characteristic peaks corresponding to magnetite (Fe_3O_4) at $2\theta = \sim30.2°$, 35.5°, 43.2°, 53.6°, 57.3°, and 62.8°. Evidently, these spectral peaks are associated with the (220), (311), (400), (422), (511), and (440) Miller indices, respectively (Fig. 3B). Furthermore, these peaks in the Fe_{12h} spectra confirm the formation of a cubic spinel magnetite (Fe_3O_4) structure during the 12 h HTC process. Lastly, the Fe_{12h} spectra aligns with the Joint Committee on Powder Diffraction Standards reference card (No. 75-0033).[11,47]

Regarding the 6 h HTC process shown in Fig. 3B, the XRD spectra illustrated the production of maghemite (Fe_2O_3) hydrochar. The maghemite (Fe_2O_3) hydrochar is characterized by shorter peak intensity, indicating smaller crystallite sizes and potential structural disorder. The presence of broad peaks at lower angles suggests the presence of graphitic carbon in the sample, likely from HTC byproducts. Crystallite size estimation using the Scherrer equation (eqn (4)) suggests that the magnetite (Fe_3O_4) hydrochar in the 12 h reaction sample has a larger crystallite size (~11.4 nm) than that in the 6 h sample (~10.3 nm), as evidenced by sharper, more defined peaks. The higher intensity of magnetite (Fe_3O_4) peaks in the 12 h sample suggests increased crystallinity due to a longer residence time, facilitating greater phase transformation from maghemite (Fe_2O_3) to magnetite (Fe_3O_4). In this light, a longer reaction time (>6 h) during HTC can produce more magnetite (Fe_3O_4) hydrochar.

$$D = \frac{k\lambda}{\beta \cos \theta} \quad (4)$$

Eqn (4) presents the Scherrer equation for crystallite size estimation, where D is the crystallite size (nm), k is the Scherrer constant (typically 0.89 for spherical nanoparticles), λ is the wavelength of CuKα radiation (0.15406 nm), β is the full width at half maximum of the diffraction peak (radians) and θ is the Bragg angle (°).

3.2.3 SEM images of MNP hydrochar

3.2.3.1 SEM images of MNP hydrochar after 6 h of HTC reaction. The MNP hydrochar was analyzed by SEM imaging to follow the changes in their surface morphology, structural transformation, and particle distribution to elucidate objective 3 further. When observed under a scanning electron microscope with a view field of 9.23 μm to 1.94 nm, the material's microstructure appears irregularly shaped (Fig. 4A–D). This is unlike the well-defined MNPs synthesized *via* co-precipitation methods.[26,46,47] Hence, HTC-fabricated MNPs tend to form irregularly shaped aggregates, consistent with the magnetite (Fe_3O_4)–biochar composites synthesized in previous studies.[29,41] The HTC-fabricated MNP microstructure consists of heterogeneous, agglomerated clusters with a rough and porous surface texture.

Despite the 6 h HTC reaction time, the surface morphology does not show significant refinement, implying that particle growth is incomplete or that secondary nucleation is occurring concurrently with carbonization. This aligns with the literature on hydrothermally synthesized MNPs, where longer reaction times (*e.g.*, 12 h or more) improve crystallinity and increase agglomeration.[12,30,33] The dense, rock-like appearance observed in the hydrochar and its characteristic black coloration suggest partial carbonization of residual organic matter, likely due to incomplete degradation of feedstock components (Fig. 4).

We utilized ImageJ, an open-source image-analyzing software developed by the U.S. National Institutes of Health (NIH), to aid in estimating the hydrochar MNP size. The MNP hydrochar size from the SEM images in Fig. 4 indicates that primary maghemite (Fe_2O_3) hydrochar ranges from 200 nm to ~1.2 μm; therefore, agglomerated clusters extend into the micrometer range. Compared to co-precipitation methods, which yield more uniform MNPs (~10–50 nm),[12,32] HTC results in a broader size distribution and greater heterogeneity. This variation in size and morphology could impact the adsorption efficiency, as smaller nanoparticles typically provide a higher surface area, while larger clusters may enhance magnetic separation capabilities.

Furthermore, porous structural characteristics observed in SEM images could enhance the adsorption performance in wastewater treatment, particularly for applications requiring magnetic separability and high surface interaction. However, the degree of particle aggregation may limit dispersion stability, requiring further optimization to prevent excessive clustering.

© 2025 The Author(s). Published by the Royal Society of Chemistry

Open Access Article. Published on 18 junio 2025. Downloaded on 30/01/2026 01:29:39 p. m..
This article is licensed under a Creative Commons Attribution-NonCommercial 3.0 Unported Licence.

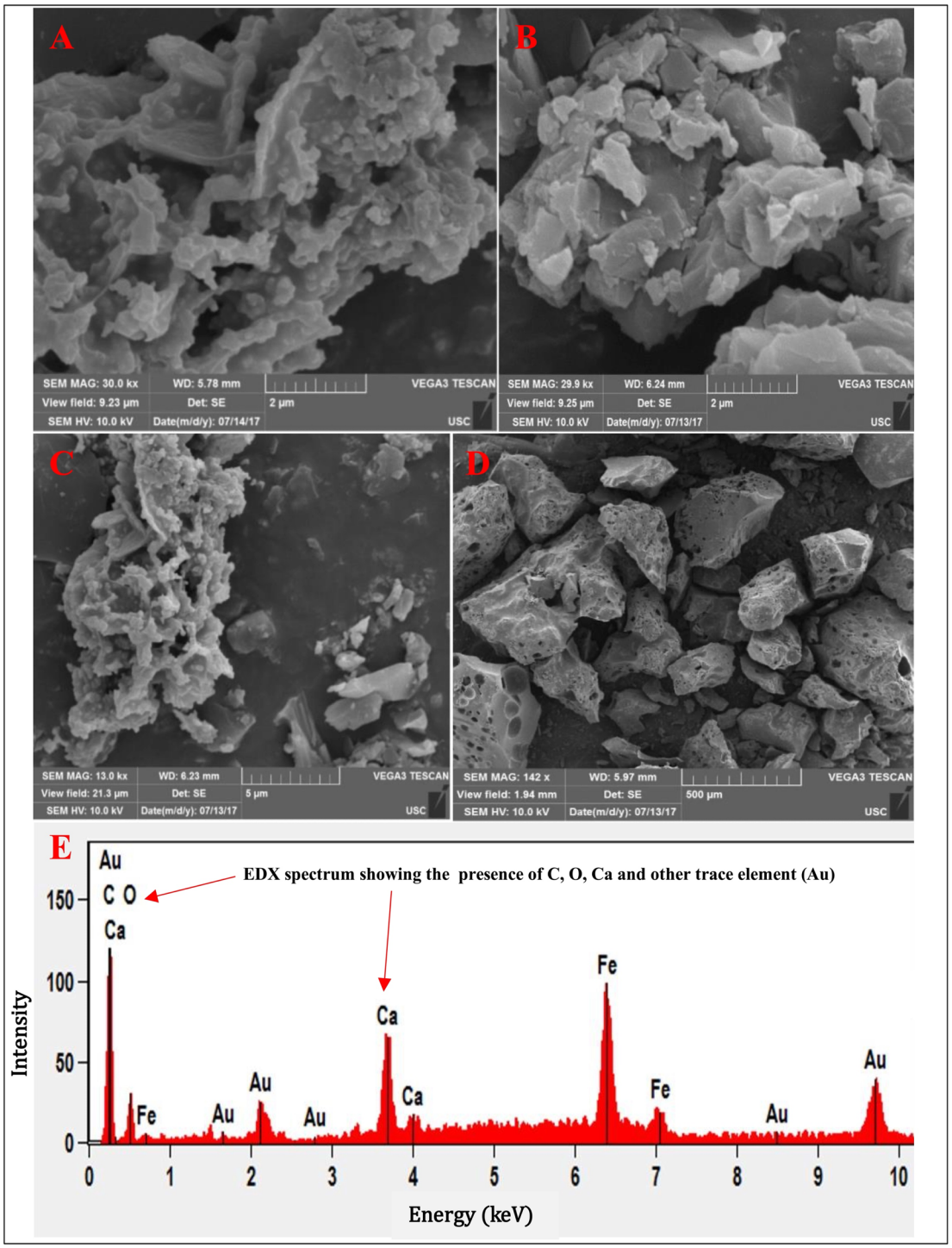

Fig. 4 (A–E) SEM micrographs and accompanying EDX elemental analysis illustrating the morphology of the MNP hydrochar obtained after 6 h of HTC. The images were captured at view fields of 9.23 µm, 9.25 µm, 21.3 µm, and 1.94 mm, highlighting the MNP hydrochar's aggregated microstructure and elemental composition.

These findings reinforce HTC as a viable yet structurally inconsistent fabrication route for MNPs, necessitating modifications in reaction parameters to control particle homogeneity.

3.2.3.2 SEM images of MNP hydrochar after 12 h of HTC reaction. Following the characterization of the 6 h HTC reaction products, the reaction time was extended to 12 h to examine its impact on the morphology and overall structural integrity of the MNP hydrochar. The SEM images in Fig. 5a–d captured at the 9.23 µm to 1.94 nm view field illustrate significant textural and morphological changes in the 12 h HTC-derived MNP hydrochar compared to that fabricated with a shorter reaction duration. The estimated size of the MNP hydrochar obtained after

Open Access Article. Published on 18 junio 2025. Downloaded on 30/01/2026 01:29:39 p. m..
This article is licensed under a Creative Commons Attribution-NonCommercial 3.0 Unported Licence.

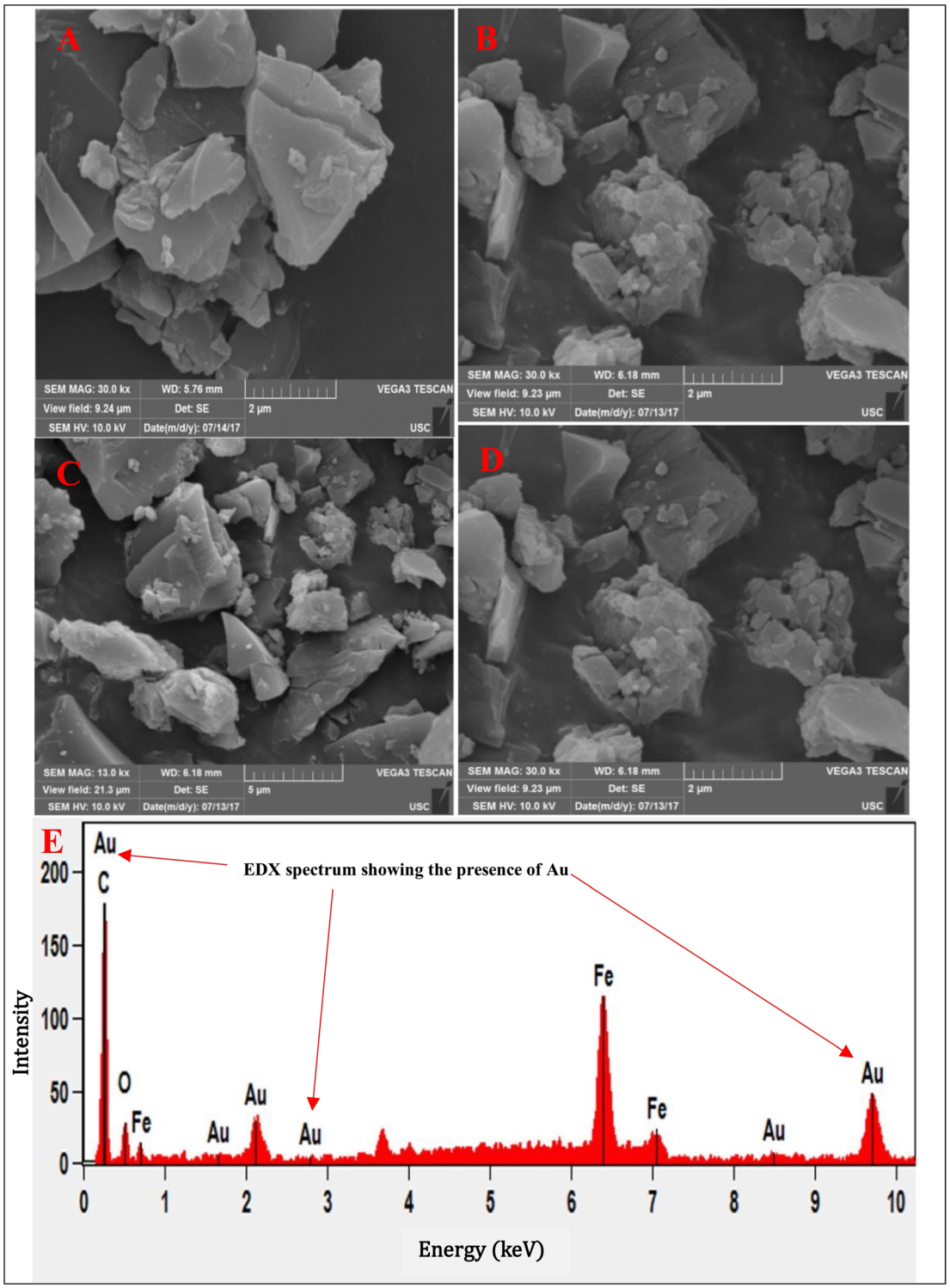

Fig. 5 (A–E). SEM micrographs and the corresponding EDX elemental analysis illustrating the morphology of the MNP hydrochar obtained after 12 h of HTC. The images were captured at view fields of 9.24 µm, 9.23 µm, 21.3 µm, and 9.23 mm, showcasing more compact and crystalline features of the MNP hydrochar.

12 h of reaction time ranged from 500 nm to ~1.2 µm. Notably, the microstructure of the 12 h HTC-derived MNP hydrochar exhibits a more defined crystalline nature with visibly larger and more uniformly shaped agglomerates. This trend is in alignment with the corresponding XRD data (refer to Section 3.2.2), indicating a phase transition from maghemite (Fe_2O_3) to magnetite (Fe_3O_4), suggesting a more complete transformation of Fe oxides under prolonged HTC conditions.

At lower magnifications, the particles appear less porous and more compacted, with a reduction in the highly irregular,

© 2025 The Author(s). Published by the Royal Society of Chemistry

Open Access Article. Published on 18 junio 2025. Downloaded on 30/01/2026 01:29:39 p. m..
This article is licensed under a Creative Commons Attribution-NonCommercial 3.0 Unported Licence.

amorphous structures observed in the 6 h HTC fabricated MNP hydrochar. This indicates that an extended reaction time facilitated further nucleation and growth of the magnetite (Fe_3O_4) crystals, leading to better-defined particle boundaries and reduced structural heterogeneity. Such observations are consistent with previous studies on HTC-derived Fe–O composites, where increased reaction durations enhanced crystal growth and minimized amorphous carbon phases.[30,33,51]

High-magnification SEM imaging reveals that the degree of particle agglomeration is more pronounced, likely due to the enhanced magnetic interactions among the magnetite (Fe_3O_4) nanoparticles. This aggregation behavior is commonly reported in HTC-fabricated Fe–O materials, where the strong dipole–dipole attraction between magnetite (Fe_3O_4) hydrochar leads to cluster formation. The nanoparticles' surface also appears smoother compared to the 6 h HTC MNP hydrochar, signifying a reduction in residual organic material from the feedstock, which aligns with the observed more blackish coloration of the final product.

Furthermore, the more compacted and less porous nature of the 12 h HTC MNP hydrochar could affect the adsorption efficiency in environmental applications. While a denser structure may result in a lower specific surface area, the enhanced crystallinity and reduced organic impurities may improve the material's stability and magnetic separation efficiency. This is particularly relevant for applications in wastewater treatment, where magnetic separation is a key factor in recovering the adsorbent after contaminant removal.

We recognize that extending the HTC reaction time from 6 to 12 h markedly improved the crystallinity, particle uniformity, and reduction of residual organic matter in the MNP hydrochar (Fig. 5). However, the increased particle compaction and aggregation suggest that additional optimization—such as surface modification or dispersing agents—may be necessary to balance structural integrity with surface accessibility for adsorption-based applications.

3.2.4 Elemental analysis of MNP hydrochar. As a final component of objective 3, EDX was employed to determine the elemental composition of the MNP hydrochar and to corroborate the presence and distribution of key elements associated with magnetite (Fe_3O_4) and maghemite (Fe_2O_3) hydrochar. Elemental Fe and carbon contents of the MNP hydrochar is often carefully considered because the more carbon the MNP hydrochar possesses, the greater its energy value and adsorption capability.[52–55] Also, more carbon in the MNP hydrochar is preferable to produce carbon-based materials for carbon sequestration and soil amendment.[52–55] Fe produced in the MNP hydrochar was high due to the main composition of the HTC feedstock. This led to the present study's successful formation of magnetite (Fe_3O_4) and maghemite (Fe_2O_3). Table 3 illustrates the weight% of each element in the fabricated MNP hydrochar.

Carbon was the most abundant element in the fabricated MNPs hydrochar. The weight% of carbon in the MNP hydrochar increased as the reaction time increased (*i.e.*, from 6 h to 12 h). The increased trend suggests that a more complete carbonization of the product can be achieved at a high reaction residence time.[56] Other trace elements—such as calcium (Ca) and gold (Au)—are found in negligible quantities in the MNP hydrochar (refer to Fig. 4E and 5E). The presence of Au is due to gold-sputtering to enhance the SEM imaging with the Hitachi TM-3000 (Tokyo, Japan) instrument.

Table 3 Weight% of elements present in MNP hydrochar after 6 h and 12 h of HTC reaction

HTC reaction time (h)	HTC (°C)	C (%)	O (%)	F (%)	Fe (%)	N (%)
6	275	80.9	56.4	0.0	38.0	1.50
12		71.8	12.7	6.3	37.4	0.0

3.3 Sustainability of MNP fabrication: comparative analysis

We herein meet objective 4 of this present study by presenting a complete LCA of three (3) common MNP production routes—HTC, pyrolysis/gasification, and co-precipitation—focusing on the product stage of each. As depicted in Fig. 6, the analysis covers ten (10) impact categories, offering a comparative view of the environmental performance of these fabrication routes. Scenario 1, which represented the HTC route for MNP fabrication, is sustainable in five (5) impact categories, whereas co-precipitation (*i.e.*, scenario 3) ranked the most sustainable in the other five (5). Scenario 2, pyrolysis/gasification, ranked the worst and was unsustainable in all ten (10) impact categories.

Furthermore, a point-to-point explanation of the LCA impact results is presented in Section 4 of the ESI.† These explanations thoroughly provide critical insights into the advantages, disadvantages, and process mechanisms resulting in the impact categories output of Fig. 6. Next, we interpret the impact categories results further.

3.3.1 Sustainability assessment. A complete LCA analysis involves the interpretation of the environmental impact categories for effective decision-making, sustainability assessment, and comparative evaluation of alternative process routes. The sustainability interpretation evaluation of the three (3) MNP fabrication routes—HTC, pyrolysis/gasification, and co-precipitation—was conducted using a ranking-based framework derived from the LCA impact category scores (Fig. 7).

The environmental impact ranking matrix revealed that HTC demonstrated the highest environmental sustainability, achieving the best performance (ranked 1st) in five (5) out of the ten (10) impact categories (see Fig. 7). Additionally, HTC achieved an overall lowest total score of 15 and an average environmental impact score of 1.5, positioning it as the most sustainable fabrication pathway.

Co-precipitation ranked second overall, performing best in the other five (5) impact categories, with a total score of 16 and an average impact score of 1.6. Conversely, pyrolysis/gasification was consistently the least sustainable, ranking worst (rank 3) across 9 out of 10 impact categories and recording the highest total score (29) and average impact score (2.9).

These findings highlight the relative environmental advantages of HTC, offering a more sustainable route for MNP

Open Access Article. Published on 18 junio 2025. Downloaded on 30/01/2026 01:29:39 p. m..
This article is licensed under a Creative Commons Attribution-NonCommercial 3.0 Unported Licence.

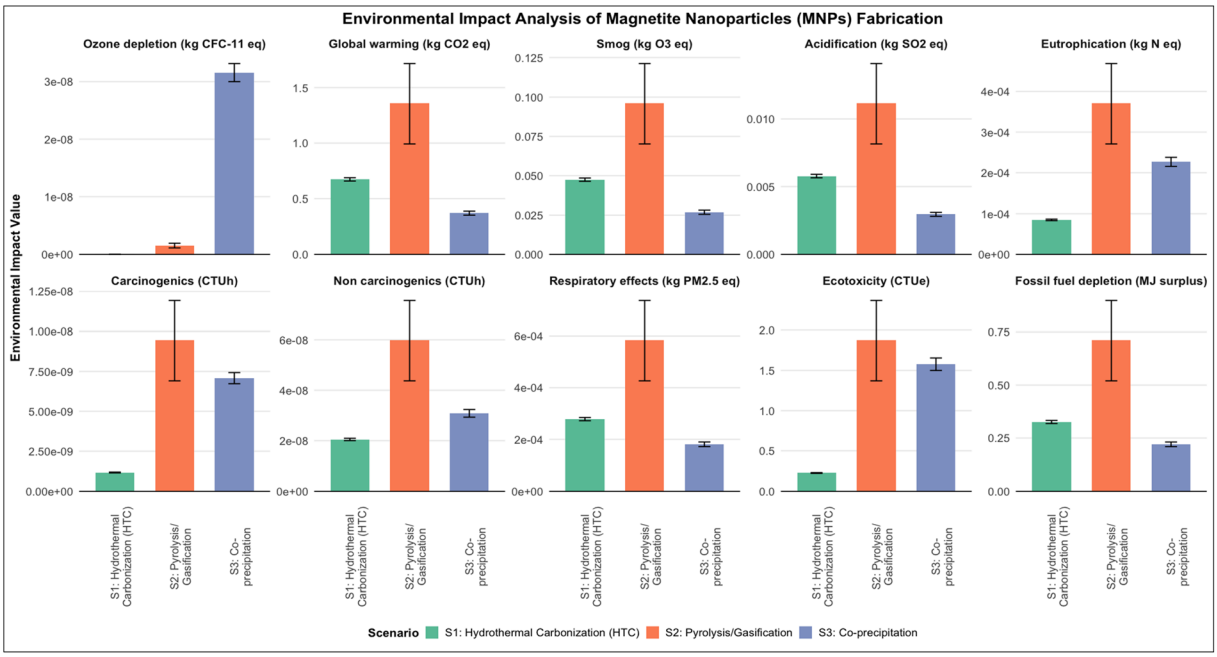

Fig. 6 LCA results for the three MNP fabrication routes—S1: hydrothermal carbonization (HTC) (colored green), S2: pyrolysis/gasification (colored orange), and S3: co-precipitation (colored blue)—evaluated using the TRACI 2.1 impact assessment method in SimaPro (Ecoinvent database). Black error bars represent the mean environmental impacts based on 10 000 Monte Carlo simulations, with error bars indicating the 95% confidence intervals to reflect uncertainty propagation across scenarios.

Environmental Impact Ranking of MNPs Fabrication Routes

Environmental Impact Category	S1: Hydrothermal Carbonization (HTC)	S2: Pyrolysis/Gasification	S3: Co-precipitation
Ozone depletion	1	2	3
Global warming	2	3	1
Smog	2	3	1
Acidification	2	3	1
Eutrophication	1	3	2
Carcinogenics	1	3	2
Non carcinogenics	1	3	2
Respiratory effects	2	3	1
Ecotoxicity	1	3	2
Fossil fuel depletion	2	3	1
Total Score	**15**	**29**	**16**
Average Environmental Impact Score	**1.5**	**2.9**	**1.6**
Overall Ranking	**1st**	**3rd**	**2nd**
Legend	*1*	*2*	*3*
	Best	Intermediate	Worst

Fig. 7 Representation of the environmental impact ranking matrix for three (3) MNP fabrication routes: S1: hydrothermal carbonization (HTC), S2: pyrolysis/gasification, and S3: co-precipitation. Rankings were assigned for each impact category based on the relative magnitude of environmental burdens derived from Life Cycle Assessment (LCA), where 1 = best (lowest impact), 2 = intermediate, and 3 = worst (highest impact). Highlighted cells are color-coded to reflect ranking levels, with green, yellow, and red representing the best, intermediate, and worst performance. Summary rows show total scores, average impact scores, and overall rankings across all categories to aid comparative sustainability interpretation.

© 2025 The Author(s). Published by the Royal Society of Chemistry

Open Access Article. Published on 18 junio 2025. Downloaded on 30/01/2026 01:29:39 p. m..
This article is licensed under a Creative Commons Attribution-NonCommercial 3.0 Unported Licence.

synthesis than the chemical and energy-intensive pyrolysis/gasification and co-precipitation methods. The color-coded ranking matrix in Fig. 7 also visually supports this interpretation, reinforcing the environmental trade-offs inherent in each production route.

Environmental sustainability assessment of a process extends beyond matrix-based ranking LCA frameworks ensuring that the end product meets functional performance benchmarks for researchers engaged in "green" synthesis or sustainable process development is equally essential. In the subsequent section, the wastewater treatment performance of the HTC-fabricated MNP hydrochar is evaluated and comparatively assessed against MNPs produced *via* pyrolysis and co-precipitation routes.

3.4 Wastewater treatment application evaluation – batch adsorption experiments

This section evaluates the efficiency and performance in removing MB from simulated wastewater to assess the practical utility of the HTC fabricated MNP hydrochar through objective 5. UV-vis analysis revealed a broad absorption band near 395–405 nm, consistent with the characteristic ligand-to-metal charge transfer (LMCT) transition from O^{2-} to Fe^{3+}. This assignment aligns with the observed spectra and is similar to other synthesized MNPs for MB removal.[6] Additionally, a comparative adsorption evaluation was performed between the HTC-derived MNP hydrochar in this study and MNPs from pyrolysis and co-precipitation. The subsequent sections, 3.4.1 to 3.4.5, focus on the effects of pH, initial concentration, contact time, adsorption kinetics, and isotherms. Furthermore, we discuss the adsorption mechanism and reaction of MNP hydrochar.

3.4.1 Effect of pH. A solution's pH markedly influences the surface charge on the adsorbent and adsorbate, thereby dictating electrostatic interactions and, consequently, the adsorption performance.[11,44,57] In the present study, the pH varies between 3 and 11 at ambient temperature. As shown in Fig. 8A, the MB removal efficiency remains above 95% within

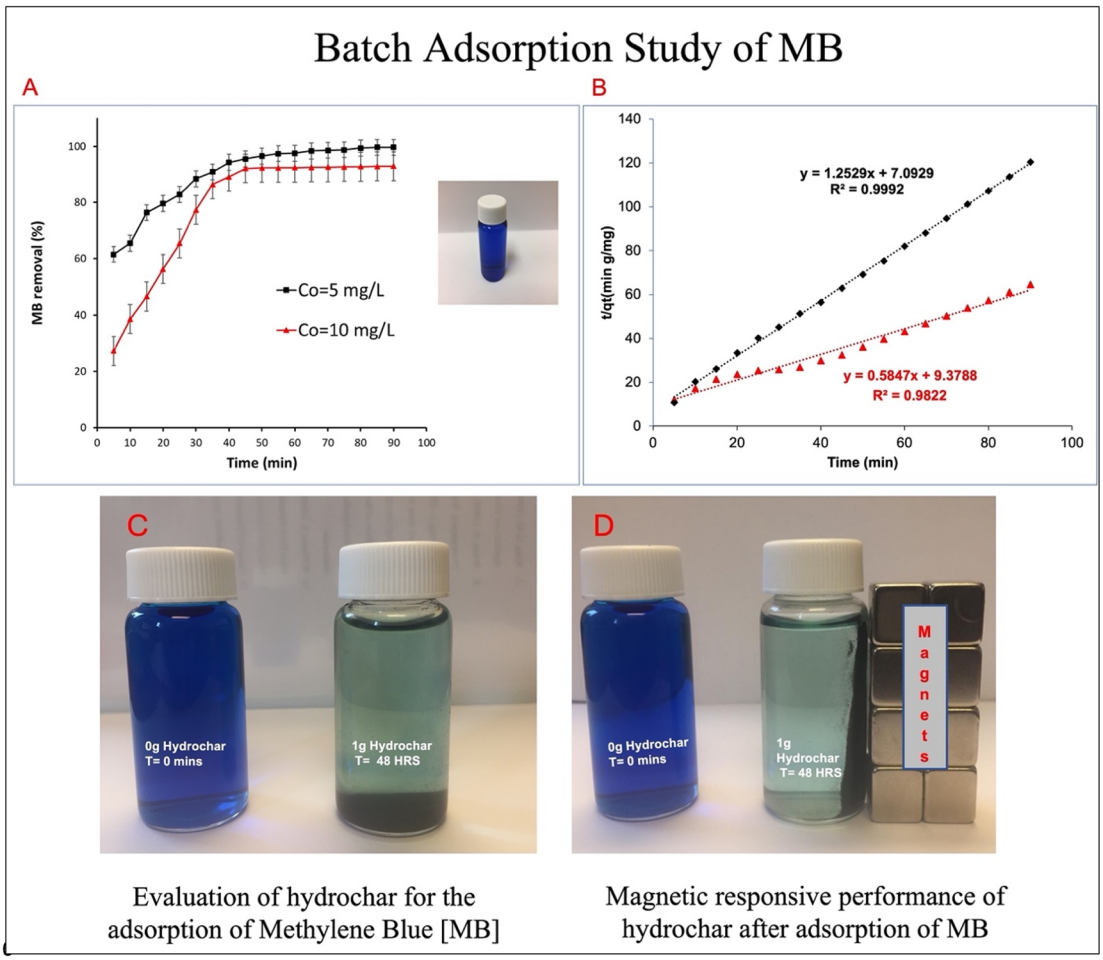

Fig. 8 (A–D) MB removal efficiency, adsorption kinetics of MNP hydrochar, and qualitative presentation of MNP hydrochar MB adsorption study. (A) MB removal efficiency over time at two initial concentrations (5 mg L^{-1} and 10 mg L^{-1}), showing rapid uptake within 30 minutes and equilibrium in 60 minutes. (B) Pseudo-second-order kinetic model fitting adsorption data, indicating strong correlation ($R^2 > 0.9$) and suggesting a chemisorption-dominant mechanism. (C) Visual comparison of MB solution before and after treatment, with the right vial (1 g MNP hydrochar) showing clear decolorization relative to the untreated control (0 g MNP hydrochar). (D) Magnetic separation demonstration of MB-loaded MNP hydrochar attracted to a magnet, confirming the magnetic recoverability of the material after dye adsorption.

© 2025 The Author(s). Published by the Royal Society of Chemistry

Open Access Article. Published on 18 junio 2025. Downloaded on 30/01/2026 01:29:39 p. m..
This article is licensed under a Creative Commons Attribution-NonCommercial 3.0 Unported Licence.

the pH range of 9–11, indicating a pronounced affinity of HTC-derived MNP hydrochar for MB under alkaline conditions. At lower pH (3–5), a modest decline in adsorption capacity (Q_e) is observed, likely due to competition between H^+ ions and the positively charged MB dye molecules for negatively charged sites on the adsorbent surface.[11] Once the pH exceeds 7, deprotonation of surface functional groups (*e.g.*, carboxyl and phenolic groups) on the MNP hydrochar enhances electrostatic attraction with MB cations.[34,58]

These results align with prior reports where MNP-based adsorbents achieve optimal dye removal at a slightly alkaline pH (8–10).[11,44,57] The high (>95%) removal in alkaline media accentuates the potential use of HTC-derived MNP hydrochar for treatment scenarios where the effluent or raw wastewater has elevated pH values.

3.4.2 Effect of initial concentration. The initial adsorbate concentration is the driving force for mass transfer, influencing the extent to which adsorption sites become saturated over time.[34] Hence, two (2) MB initial concentrations (5 mg L^{-1} and 10 mg L^{-1}) were tested in the present study. With the initial concentration of 5 mg L^{-1}, the 6 h HTC-derived MNP hydrochar exhibited a Q_e of 0.7305 mg g^{-1}, whereas increasing the concentration to 10 mg L^{-1} (and extending HTC to 12 h) enhanced the adsorption capacity to 1.38 mg g^{-1} (refer to Table 4). This increase in capacity with higher MB concentration is in line with previous literature reports on co-precipitation-derived MNPs with pyrolyzed biochar composites,[57] wherein higher initial concentrations create a stronger concentration gradient that drives MB molecules more efficiently to the adsorbent surface.[4–6]

Although some studies have reported higher Q_e values (*e.g.*, 19–183.82 mg g^{-1} for pyrolysis-derived Fe–biochar nanocomposites),[48,57,59] it is noteworthy that the adsorption kinetics in the present study remain rapid, and the overall removal efficiency is consistently above 95% at neutral to alkaline pH (Fig. 8A and Table 4). Furthermore, while the Q_e value reported in this study was lower compared to materials such as biochar, activated carbons, and zeolites with Brunauer–Emmett–Teller (BET) values exceeding 200–900 m^2 g^{-1}, it remained competitive with other similar green-synthesized MNPs with reported BET values of 7–150 m^2 g^{-1}.[12,59,60] This wide range can be due to fabrication methods and initial feedstock properties. We estimate the BET value of our MNP hydrochar to be in a similar range. Lastly, from an application standpoint, achieving high removal percentages—especially at lower-to-moderate MB concentrations—can be advantageous for certain industrial or municipal wastewater streams.[20,61,62]

3.4.3 Effect of contact time of MNP hydrochar as an adsorbent. Adsorption of MB onto the HTC-derived MNP hydrochar occurred biphasically: an initial rapid uptake followed by a slower approach to equilibrium. This trend is discussed in similar studies using MB.[34,41] Equilibrium is achieved within approximately 90 minutes for both 5 and 10 mg L^{-1} initial concentrations, which is relatively fast compared to some pyrolyzed adsorbents (see Fig. 8A and B).[46,57] As shown in Fig. 8A, during the initial phase (within the first 30 minutes), abundant vacant sites on the external surface and the accessible

Table 4 Adsorption study model for MNP hydrochar in MB removal *vs.* other recent studies

Initial color/dye concentration (mg L^{-1})	Fabrication method	Feedstock	Adsorption evaluation kinetic model	K_2 (g mg^{-1} min^{-1})	R^2	Q_e (calculated) (mg g^{-1})	References
5	HTC @ 6 h	Waste iron supplement	Pseudo-second-order	1.2529	0.9992	0.7305	This study
10	HTC @ 12 h	Waste iron supplement	Pseudo-second-order	0.5847	0.9822	1.38	This study
5	Co-precipitation	Jengkol peel extract + ferric salts + chemical reagents	Ho's pseudo-first-order	0.00098	0.9996	1428.6	11
15	Co-precipitation	Jengkol peel extract	Ho's pseudo-first-order	0.00123	0.9996	1428.6	11
10	Co-precipitation	Ferric salts + chemical reagents	Pseudo-second-order	N/A	0.9295	19	5
20	Co-precipitation	Ferric salts + chemical reagents	Pseudo-second-order	N/A	0.9295	36.2	5
10	Co-precipitation	*Cordia myxa* leaf extract + ferric salts + chemical reagents	Pseudo-second-order	0.009	0.9947	21.07	48
15	Pyrolysis	Eucalyptus sawdust + organic acids	Pseudo-second-order	0.0416	1	19.841	44
20	Pyrolysis	Eucalyptus sawdust + organic acids	Pseudo-second-order	0.0263	1	26.525	44
25	Pyrolysis	Eucalyptus sawdust + organic acids	Pseudo-second-order	0.0131	1	32.787	44
30	Pyrolysis	Eucalyptus sawdust + organic acids	Pseudo-second-order	0.00638	1	39.216	44
10[a]	Pyrolysis + co-precipitation	Coconut shell + chemical reagents	Pseudo-second-order	0.049	0.9695	3.38	16
200	Pyrolysis + co-precipitation	Rice husk + chemical reagents	Pseudo-second-order	6 055 750.89	0.9998	183.82	57

[a] Note: all studies in Table 4 utilized MB as the initial color or dye to be removed except Cazetta *et al.* (2016), where the sunset yellow dye was utilized.[16]

© 2025 The Author(s). Published by the Royal Society of Chemistry

Open Access Article. Published on 18 junio 2025. Downloaded on 30/01/2026 01:29:39 p. m..
This article is licensed under a Creative Commons Attribution-NonCommercial 3.0 Unported Licence.

pores of the MNP hydrochar allowed for swift MB binding. As these sites became occupied, intraparticle diffusion and repulsive forces among adsorbed MB molecules slowed the adsorption rate, culminating in equilibrium.

This rapid kinetics demonstrates that HTC-derived MNP adsorbents, synthesized from waste Fe supplements, have a practical advantage in situations requiring prompt contaminant removal. Industrial treatment processes like continuous-flow systems can capitalize on shorter residence times, reducing the overall operational costs.

3.4.4 Adsorption kinetics and isotherms. In the context of wastewater treatment system design, adsorption kinetics and isotherm modeling are critical tools for evaluating the adsorbent mechanisms and efficiency of pollutant uptake. Kinetic modeling provides insight into the underlying rate-limiting steps. In our kinetic modeling analysis, the pseudo-second-order model described the experimental data more accurately than the pseudo-first-order model. The pseudo-second-order model equation was then utilized in this study following other similar MNP adsorption studies (refer to Table 4).[5,44,48,63]

As presented in Table 4, the rate constants (K_2) for the 6 h and 12 h HTC-derived hydrochar were 1.2529 g mg^{-1} min^{-1} and 0.5847 g mg^{-1} min^{-1}, respectively, with correlation coefficients (R^2) exceeding 0.98 (see Fig. 8B). These results suggest chemisorption as the principal process for MB adsorption, involving valence forces or electron sharing between the adsorbent surface sites and the MB molecules.

The adsorption capacities (Q_e) for the MNP hydrochar in this study were lower than those reported for co-precipitation or pyrolysis + coprecipitation derived MNP adsorbents (*i.e.*, 19 and 20 mg g^{-1} at initial MB concentrations of 10 and 15 mg L^{-1}, respectively).[4,44] However, the relatively high k_2 values reflect rapid kinetic behavior, a critical advantageous parameter for large-scale treatment systems that require quick throughput. Isotherm modeling (*e.g.*, Langmuir and Freundlich) could further confirm whether MB adsorption on the MNP hydrochar follows monolayer or multilayer adsorption, although preliminary data indicate the strong applicability of monolayer models at the tested concentrations.[11]

3.4.5 Adsorption mechanisms. FTIR analysis of the present study (refer to Section 3.2.1) and previous literature collectively indicate that electrostatic attraction, hydrogen bonding, and π–π interactions are key drivers of MB sequestration on MNP hydrochar.[12,32,46,53,54,58] Under alkaline conditions, the deprotonation of functional groups—carboxylic (–COOH), phenolic (–OH), and other acidic sites—renders the adsorbent surface negatively charged, reinforcing electrostatic coupling with the cationic MB molecules.[12,32,46,53,54,58] The Fe–O oxide moieties can also facilitate surface complexation, further increasing the adsorption affinity.[11,30,48] Additionally, π–π stacking between the aromatic rings of MB and the graphitic domains in MNP hydrochar contributes to the overall adsorption capacity.[41]

While the equilibrium adsorption capacities of HTC-derived MNP hydrochar are somewhat lower than those attained by certain co-precipitation or pyrolyzed adsorbents (refer to Table 4), advantages such as faster kinetic responses and greater sustainability ranking position them as viable candidates for sustainable water treatment applications. Given that real-world systems often involve moderate dye or color concentrations and demand quick treatment times, these MNP hydrochar could play a pivotal role in scalable and sustainable wastewater remediation processes.

3.5 Implications and future research directions

This study demonstrates that the fabrication pathways for magnetite (Fe_3O_4) and maghemite (Fe_2O_3) nanoparticles—*via* HTC, pyrolysis/gasification, and co-precipitation—differ significantly in terms of energy demands, chemical inputs, and environmental burdens. Among these, HTC emerged as the most environmentally favorable route. To further enhance its sustainability, future research should focus on integrating diverse Fe-rich feedstocks, renewable energy sources (*e.g.*, solar thermal input) and optimizing key reaction parameters, such as temperature and residence time, to reduce fossil fuel depletion, acidification potential, and respiratory impacts. Additionally, expanding the LCA system boundaries to include infrastructure requirements and end-of-life scenarios will provide a more comprehensive understanding of each method's long-term sustainability and technological viability.

4 Conclusions

In the present study, expired Fe dietary supplements were successfully converted *via* HTC into MNP hydrochar, predominantly comprising magnetite (Fe_3O_4) and maghemite (Fe_2O_3) with comparable magnetic spinel structures to Fe nanoparticles from previous studies that utilized co-precipitation. The straightforward stainless steel reactor setup demonstrated that extending the HTC reaction time from 6 to 12 h increased the fixed carbon content in the hydrochar but decreased the overall yield. This underscores the balance between maximizing carbon retention and driving off volatile components.

Our HTC process highlights a viable pathway for converting Fe-rich waste materials into value-added nanoparticles with a broad potential in remediation or advanced materials. Moreover, the relatively mild operating conditions (275 °C) present fewer safety concerns than higher-temperature pyrolytic methods. However, further characterization of the liquid and gas phases remains vital for elucidating chemical transformations and exploring beneficial reuses (*e.g.*, syngas for energy recovery).

From an LCA perspective, the results suggested that the HTC process is most sustainable, by a close margin, compared to the co-precipitation method. Hence, HTC minimizes environmental burdens across several impact categories through its straightforward operating strategies. Meanwhile, MB adsorption trials confirm that HTC-derived MNP hydrochar can effectively remove contaminants, showcasing its suitability for wastewater treatment. Ultimately, selection of the MNP fabrication method will mainly depend on the quantity of MNPs needed and the specific application. Both co-precipitation and HTC can be even more sustainable, and future research should optimize reactor designs and scalability to fully realize the most appropriate route for sustainable, large-scale production of MNPs.

Open Access Article. Published on 18 junio 2025. Downloaded on 30/01/2026 01:29:39 p. m.. This article is licensed under a Creative Commons Attribution-NonCommercial 3.0 Unported Licence.

Abbreviations

AP	Acidification potential
EDX	Energy dispersive X-ray spectroscopy
EP	Eutrophication potential
FTIR	Fourier Transform Infrared Spectroscopy
GWP	Global warming potential
HTC	Hydrothermal carbonization
LCA	Life cycle assessment/analysis
MB	Methylene blue
MNPs	Magnetite or Maghemite nanoparticles
ODP	Ozone depletion potential
SEM	Scanning Electron Microscopy
SFP	Smog formation potential
XRD	X-ray diffraction

Data availability

All data collected during the study are presented in the submitted manuscript and the ESI.†

Author contributions

All authors contributed to the study conception, design, data collection and analysis, and manuscript development. Ahmed Ibrahim Yunus and Dr Samuel Darko performed material preparation, data collection, and analysis. Ahmed Ibrahim Yunus and Dr Samuel Darko wrote the first draft of the manuscript, and all authors commented on previous versions. All authors read and approved the final manuscript.

Conflicts of interest

The authors have declared no conflict of interest.

Acknowledgements

The authors would like to acknowledge the great support and assistance from Mr Habib Alsoudani, Dr Nicole D. Berge, Dr Wen Cun, and Dr Changyong Qin of The University of South Carolina. This research was funded by the U.S. Department of Energy Grant no. 2088-25 and, in part, by the Renewable Bi-Product Institute (RBI). Declaration of generative AI and AI-assisted technologies in the writing process. While preparing this work, the authors used Grammarly to check grammar and ensure reading clarity. After using this tool, the authors reviewed and edited the content as needed and take full responsibility for the publication's content.

References

1 V. Balaram, Rare Earth Elements: A Review of Applications, Occurrence, Exploration, Analysis, Recycling, and Environmental Impact, *Geosci. Front.*, 2019, **10**(4), 1285–1303, DOI: **10.1016/j.gsf.2018.12.005**.

2 P. Dong, T. Zhang, H. Xiang, X. Xu, Y. Lv, Y. Wang and C. Lu, Controllable Synthesis of Exceptionally Small-Sized Superparamagnetic Magnetite Nanoparticles for Ultrasensitive MR Imaging and Angiography, *J. Mater. Chem. B*, 2021, **9**(4), 958–968, DOI: **10.1039/D0TB02337J**.

3 M. Yaghoobi and F. Asjadi, Selective Synthesis of Mesoporous Magnetic Iron Oxide Nanoparticles *via* Green Approach: Highly Efficient Adsorption of Malachite Green, *Trans. Indian Inst. Met.*, 2025, **78**(1), 19, DOI: **10.1007/s12666-024-03525-3**.

4 F. S. Braim, N. N. A. Nik Ab Razak, A. A. Aziz, M. A. Dheyab and L. Q. Ismael, Rapid Green-Assisted Synthesis and Functionalization of Superparamagnetic Magnetite Nanoparticles Using *Sumac* Extract and Assessment of Their Cellular Toxicity, Uptake, and Anti-Metastasis Property, *Ceram. Int.*, 2023, **49**(5), 7359–7369, DOI: **10.1016/j.ceramint.2022.10.207**.

5 S. T. Aly, A. Saed, A. Mahmoud, M. Badr, S. S. Garas, S. Yahya and K. H. Hamad, Preparation of Magnetite Nanoparticles and Their Application in the Removal of Methylene Blue Dye from Wastewater, *Sci. Rep.*, 2024, **14**(1), 20100, DOI: **10.1038/s41598-024-69790-w**.

6 M. S. Akhtar, S. Fiaz, S. Aslam, S. Chung, A. Ditta, M. A. Irshad, A. M. Al-Mohaimeed, R. Iqbal, W. A. Al-onazi, M. Rizwan and Y. Nakashima, Green Synthesis of Magnetite Iron Oxide Nanoparticles Using *Azadirachta indica* Leaf Extract Loaded on Reduced Graphene Oxide and Degradation of Methylene Blue, *Sci. Rep.*, 2024, **14**(1), 18172, DOI: **10.1038/s41598-024-69184-y**.

7 A.-G. Niculescu, C. Chircov and A. M. Grumezescu, Magnetite Nanoparticles: Synthesis Methods – A Comparative Review, *Methods*, 2022, **199**, 16–27, DOI: **10.1016/j.ymeth.2021.04.018**.

8 R. Bhole, D. Gonsalves, G. Murugesan, M. K. Narasimhan, N. R. Srinivasan, N. Dave, T. Varadavenkatesan, R. Vinayagam, M. Govarthanan and R. Selvaraj, Superparamagnetic Spherical Magnetite Nanoparticles: Synthesis, Characterization and Catalytic Potential, *Appl. Nanosci.*, 2023, **13**(9), 6003–6014, DOI: **10.1007/s13204-022-02532-4**.

9 V. S. Patil, S. S. Thoravat, S. S. Kundale, T. D. Dongale, P. S. Patil and S. A. Jadhav, Synthesis and Testing of Polyaniline Grafted Functional Magnetite (Fe3O4) Nanoparticles and rGO Based Nanocomposites for Supercapacitor Application, *Chem. Phys. Lett.*, 2023, **814**, 140334, DOI: **10.1016/j.cplett.2023.140334**.

10 G. Magnacca, A. Allera, E. Montoneri, L. Celi, D. E. Benito, L. G. Gagliardi, M. C. Gonzalez, D. O. Mártire and L. Carlos, Novel Magnetite Nanoparticles Coated with Waste-Sourced Biobased Substances as Sustainable and Renewable Adsorbing Materials, *ACS Sustain. Chem. Eng.*, 2014, **2**(6), 1518–1524, DOI: **10.1021/sc500213j**.

11 M. Rahmayanti, A. Nurul Syakina, I. Fatimah and T. Sulistyaningsih, Green Synthesis of Magnetite Nanoparticles Using Peel Extract of Jengkol (*Archidendron Pauciflorum*) for Methylene Blue Adsorption from Aqueous

© 2025 The Author(s). Published by the Royal Society of Chemistry

Open Access Article. Published on 18 junio 2025. Downloaded on 30/01/2026 01:29:39 p. m.. This article is licensed under a Creative Commons Attribution-NonCommercial 3.0 Unported Licence.

Media, *Chem. Phys. Lett.*, 2022, **803**, 139834, DOI: 10.1016/j.cplett.2022.139834.

12 R. Vinayagam, V. Nagendran, G. Murugesan, L. C. Goveas, T. Varadavenkatesan, A. Samanth and R. Selvaraj, *In Situ* One-Pot Synthesis, Characterization of Magnetic Hydrochar and Its Application as Fenton-like Catalyst for the Degradation of Methylene Blue Dye, *Mater. Chem. Phys.*, 2024, **317**, 129160, DOI: 10.1016/j.matchemphys.2024.129160.

13 B. Ramalingam, T. Parandhaman, P. Choudhary and S. K. Das, Biomaterial Functionalized Graphene-Magnetite Nanocomposite: A Novel Approach for Simultaneous Removal of Anionic Dyes and Heavy-Metal Ions, *ACS Sustain. Chem. Eng.*, 2018, **6**(5), 6328–6341, DOI: 10.1021/acssuschemeng.8b00139.

14 X. Luo, X. Lei, N. Cai, X. Xie, Y. Xue and F. Yu, Removal of Heavy Metal Ions from Water by Magnetic Cellulose-Based Beads with Embedded Chemically Modified Magnetite Nanoparticles and Activated Carbon, *ACS Sustain. Chem. Eng.*, 2016, **4**(7), 3960–3969, DOI: 10.1021/acssuschemeng.6b00790.

15 T. K. Sahu, S. Arora, A. Banik, P. K. Iyer and M. Qureshi, Efficient and Rapid Removal of Environmental Malignant Arsenic(III) and Industrial Dyes Using Reusable, Recoverable Ternary Iron Oxide – ORMOSIL - Reduced Graphene Oxide Composite, *ACS Sustain. Chem. Eng.*, 2017, **5**(7), 5912–5921, DOI: 10.1021/acssuschemeng.7b00632.

16 A. L. Cazetta, O. Pezoti, K. C. Bedin, T. L. Silva, A. Paesano Junior, T. Asefa and V. C. Almeida, Magnetic Activated Carbon Derived from Biomass Waste by Concurrent Synthesis: Efficient Adsorbent for Toxic Dyes, *ACS Sustain. Chem. Eng.*, 2016, **4**(3), 1058–1068, DOI: 10.1021/acssuschemeng.5b01141.

17 R. Nisticò, F. Franzoso, F. Cesano, D. Scarano, G. Magnacca, M. E. Parolo and L. Carlos, Chitosan-Derived Iron Oxide Systems for Magnetically Guided and Efficient Water Purification Processes from Polycyclic Aromatic Hydrocarbons, *ACS Sustain. Chem. Eng.*, 2017, **5**(1), 793–801, DOI: 10.1021/acssuschemeng.6b02126.

18 S. Mirshahghassemi, B. Cai and J. R. Lead, Evaluation of Polymer-Coated Magnetic Nanoparticles for Oil Separation under Environmentally Relevant Conditions: Effect of Ionic Strength and Natural Organic Macromolecules, *Environ. Sci.:Nano*, 2016, **3**(4), 780–787, DOI: 10.1039/C5EN00282F.

19 S. Mirshahghassemi and J. R. Lead, Oil Recovery from Water under Environmentally Relevant Conditions Using Magnetic Nanoparticles, *Environ. Sci. Technol.*, 2015, **49**(19), 11729–11736, DOI: 10.1021/acs.est.5b02687.

20 N. Sh. El-Gendy and H. N. Nassar, Biosynthesized Magnetite Nanoparticles as an Environmental Opulence and Sustainable Wastewater Treatment, *Sci. Total Environ.*, 2021, **774**, 145610, DOI: 10.1016/j.scitotenv.2021.145610.

21 I. K. Rind, M. Tuzen, A. Sarı, M. F. Lanjwani, N. Memon and T. A. Saleh, Synthesis of TiO2 Nanoparticles Loaded on Magnetite Nanoparticles Modified Kaolinite Clay (KC) and Their Efficiency for As(III) Adsorption, *Chem. Eng. Res. Des.*, 2023, **191**, 523–536, DOI: 10.1016/j.cherd.2023.01.046.

22 M. Zahedifar, N. Seyedi, S. Shafiei and M. Basij, Surface-Modified Magnetic Biochar: Highly Efficient Adsorbents for Removal of Pb(II) and Cd(II), *Mater. Chem. Phys.*, 2021, **271**, 124860, DOI: 10.1016/j.matchemphys.2021.124860.

23 M. Carmona-Cabello, I. L. Garcia, D. Leiva-Candia and M. P. Dorado, Valorization of Food Waste Based on Its Composition through the Concept of Biorefinery, *Curr. Opin. Green Sustainable Chem.*, 2018, **14**, 67–79, DOI: 10.1016/j.cogsc.2018.06.011.

24 S. Yu, J. He, Z. Zhang, Z. Sun, M. Xie, Y. Xu, X. Bie, Q. Li, Y. Zhang, M. Sevilla, M.-M. Titirici and H. Zhou, Towards Negative Emissions: Hydrothermal Carbonization of Biomass for Sustainable Carbon Materials, *Adv. Mater.*, 2024, **36**(18), 2307412, DOI: 10.1002/adma.202307412.

25 I. Fatimah, N. Nurlaela, R. A. Nugraha, A. Z. Fauziyyah, N. F. Salsabila, S. Sagadevan, G. Purwiandono, G. D. Ramanda and W.-C. Oh, Zero Valent Nickel Biochar Nanocomposites from Squeezed Orange (*Citrus sinensis*) as Stable and Reusable Catalyst in Wet Peroxidation of Dye, *Mater. Chem. Phys.*, 2025, **334**, 130459, DOI: 10.1016/j.matchemphys.2025.130459.

26 F. V. Gutierrez, I. S. Lima, A. D. Falco, B. M. Ereias, O. Baffa, C. D. de A. Lima, L. I. M. Sinimbu, P. de la Presa, C. Luz-Lima and J. F. D. F. Araujo, The Effect of Temperature on the Synthesis of Magnetite Nanoparticles by the Coprecipitation Method, *Heliyon*, 2024, **10**(4), e25781, DOI: 10.1016/j.heliyon.2024.e25781.

27 H. Alhassan, V. N. Yoong, Y. W. Soon, A. Usman, M. S. A. Bakar, A. Ahmed and M. Luengchavanon, The Differential Influence of Biochar and Graphite Precursors on the Structural, Optical, and Electrochemical Properties of Graphene Oxide, *Mater. Chem. Phys.*, 2025, **329**, 130070, DOI: 10.1016/j.matchemphys.2024.130070.

28 M. S. A. Darwish, L. M. Al-Harbi and A. Bakry, Synthesis of Magnetite Nanoparticles Coated with Polyvinyl Alcohol for Hyperthermia Application, *J. Therm. Anal. Calorim.*, 2022, **147**(21), 11921–11930, DOI: 10.1007/s10973-022-11393-6.

29 Y. Jiao, Q. Xu, Y. Hu, J. Wu and X. Su, Pyrolysis Co-Activation Synthesized Magnetic Biochar for Efficient Removal of Cr(VI) from Aqueous Solution, *Mater. Chem. Phys.*, 2023, **295**, 127080, DOI: 10.1016/j.matchemphys.2022.127080.

30 J. M. M. Silva, P. E. Feuser, R. Cercená, M. Peterson and A. G. Dal-Bó, Obtention of Magnetite Nanoparticles *via* the Hydrothermal Method and Effect of Synthesis Parameters, *J. Magn. Magn. Mater.*, 2023, **580**, 170925, DOI: 10.1016/j.jmmm.2023.170925.

31 M. Masuku, L. Ouma and A. Pholosi, Microwave Assisted Synthesis of Oleic Acid Modified Magnetite Nanoparticles for Benzene Adsorption, *Environ. Nanotechnol., Monit. Manage.*, 2021, **15**, 100429, DOI: 10.1016/j.enmm.2021.100429.

32 S. Wang, Y. Zhang, T. Zhang, M. Zhao, N. Zhou, X. Hu, S. Fan and H. Xu, Layered Double Hydroxides/Biochar Composites for Adsorptive Removal of Tetracycline and Ciprofloxacin, *Mater. Chem. Phys.*, 2024, **328**, 130001, DOI: 10.1016/j.matchemphys.2024.130001.

Open Access Article. Published on 18 junio 2025. Downloaded on 30/01/2026 01:29:39 p. m.. This article is licensed under a Creative Commons Attribution-NonCommercial 3.0 Unported Licence.

33 T. J. Daou, G. Pourroy, S. Bégin-Colin, J. M. Grenèche, C. Ulhaq-Bouillet, P. Legaré, P. Bernhardt, C. Leuvrey and G. Rogez, Hydrothermal Synthesis of Monodisperse Magnetite Nanoparticles, *Chem. Mater.*, 2006, **18**(18), 4399–4404, DOI: **10.1021/cm060805r**.

34 G. Davies and J. McGregor, Hydrothermal Synthesis of Biomass-Derived Magnetic Carbon Composites for Adsorption and Catalysis, *ACS Omega*, 2021, **6**(48), 33000–33009, DOI: **10.1021/acsomega.1c05116**.

35 J. González-Arias, M. E. Sánchez, J. Cara-Jiménez, F. M. Baena-Moreno and Z. Zhang, Hydrothermal Carbonization of Biomass and Waste: A Review, *Environ. Chem. Lett.*, 2022, **20**(1), 211–221, DOI: **10.1007/s10311-021-01311-x**.

36 X. Zhuang, J. Liu, Q. Zhang, C. Wang, H. Zhan and L. Ma, A Review on the Utilization of Industrial Biowaste *via* Hydrothermal Carbonization, *Renewable Sustainable Energy Rev.*, 2022, **154**, 111877, DOI: **10.1016/j.rser.2021.111877**.

37 D. Lachos-Perez, P. César Torres-Mayanga, E. R. Abaide, G. L. Zabot and F. De Castilhos, Hydrothermal Carbonization and Liquefaction: Differences, Progress, Challenges, and Opportunities, *Bioresour. Technol.*, 2022, **343**, 126084, DOI: **10.1016/j.biortech.2021.126084**.

38 M. Cavali, N. Libardi Junior, J. D. de Sena, A. L. Woiciechowski, C. R. Soccol, P. Belli Filho, R. Bayard, H. Benbelkacem and A. B. de Castilhos Junior, A Review on Hydrothermal Carbonization of Potential Biomass Wastes, Characterization and Environmental Applications of Hydrochar, and Biorefinery Perspectives of the Process, *Sci. Total Environ.*, 2023, **857**, 159627, DOI: **10.1016/j.scitotenv.2022.159627**.

39 G. Ischia, M. Cutillo, G. Guella, N. Bazzanella, M. Cazzanelli, M. Orlandi, A. Miotello and L. Fiori, Hydrothermal Carbonization of Glucose: Secondary Char Properties, Reaction Pathways, and Kinetics, *Chem. Eng. J.*, 2022, **449**, 137827, DOI: **10.1016/j.cej.2022.137827**.

40 P. Das, S. Upadhyay, S. Dubey and K. K. Singh, Waste to Wealth: Recovery of Value-Added Products from Steel Slag, *J. Environ. Chem. Eng.*, 2021, **9**(4), 105640, DOI: **10.1016/j.jece.2021.105640**.

41 C. Wurzer and O. Mašek, Feedstock Doping Using Iron Rich Waste Increases the Pyrolysis Gas Yield and Adsorption Performance of Magnetic Biochar for Emerging Contaminants, *Bioresour. Technol.*, 2021, **321**, 124473, DOI: **10.1016/j.biortech.2020.124473**.

42 N. D. Berge, K. S. Ro, J. Mao, J. R. V. Flora, M. A. Chappell and S. Bae, Hydrothermal Carbonization of Municipal Waste Streams, *Environ. Sci. Technol.*, 2011, **45**(13), 5696–5703, DOI: **10.1021/es2004528**.

43 A. Sarrion, M. A. de la Rubia, N. D. Berge, A. F. Mohedano and E. Diaz, Comparison of Nutrient-Release Strategies in Hydrothermally Treated Digested Sewage Sludge, *ACS Sustain. Chem. Eng.*, 2023, **11**(17), 6498–6509, DOI: **10.1021/acssuschemeng.2c05870**.

44 L. Sun, D. Chen, S. Wan and Z. Yu, Performance, Kinetics, and Equilibrium of Methylene Blue Adsorption on Biochar Derived from Eucalyptus Saw Dust Modified with Citric, Tartaric, and Acetic Acids, *Bioresour. Technol.*, 2015, **198**, 300–308, DOI: **10.1016/j.biortech.2015.09.026**.

45 S. Rodríguez-Sánchez, B. Ruiz, D. Martínez-Blanco, M. Sánchez-Arenillas, M. A. Diez, I. Suárez-Ruiz, J. F. Marco, J. Blanco and E. Fuente, Sustainable Thermochemical Single-Step Process To Obtain Magnetic Activated Carbons from Chestnut Industrial Wastes, *ACS Sustain. Chem. Eng.*, 2019, **7**(20), 17293–17305, DOI: **10.1021/acssuschemeng.9b04141**.

46 K. Hayashi, H. Tomonaga, T. Matsuyama and J. Ida, Facile Synthesis, Characterization of Various Polymer Immobilized on Magnetite Nanoparticles Applying the Coprecipitation Method, *J. Appl. Polym. Sci.*, 2022, **139**(5), 51581, DOI: **10.1002/app.51581**.

47 H. Mohammadi, E. Nekobahr, J. Akhtari, M. Saeedi, J. Akbari and F. Fathi, Synthesis and Characterization of Magnetite Nanoparticles by Co-Precipitation Method Coated with Biocompatible Compounds and Evaluation of *in Vitro* Cytotoxicity, *Toxicol Rep*, 2021, **8**, 331–336, DOI: **10.1016/j.toxrep.2021.01.012**.

48 E. Ghoohestani, F. Samari, A. Homaei and S. Yosuefinejad, A Facile Strategy for Preparation of Fe_3O_4 Magnetic Nanoparticles Using Cordia Myxa Leaf Extract and Investigating Its Adsorption Activity in Dye Removal, *Sci. Rep.*, 2024, **14**(1), 84, DOI: **10.1038/s41598-023-50550-1**.

49 A. Funke and F. Ziegler, Hydrothermal Carbonization of Biomass: A Summary and Discussion of Chemical Mechanisms for Process Engineering, *Biofuels, Bioprod. Biorefin.*, 2010, **4**(2), 160–177, DOI: **10.1002/bbb.198**.

50 Z. Wang, Y. Zhai, T. Wang, C. Peng, S. Li, B. Wang, X. Liu and C. Li, Effect of Temperature on the Sulfur Fate during Hydrothermal Carbonization of Sewage Sludge, *Environ. Pollut.*, 2020, **260**, 114067, DOI: **10.1016/j.envpol.2020.114067**.

51 K. E. B. O'Neill, J. Biswakarma, R. Crane and J. M. Byrne, Recovery of Co(II), Ni(II) and Zn(II) Using Magnetic Nanoparticles (MNPs) at Circumneutral pH, *Geosci. Front.*, 2025, **12**(4), 2371–2382, DOI: **10.1039/D4EN01176G**.

52 A. S. Ouedraogo, G. Yuzhu Fu and A. I. Yunus, Treatment of Highway Stormwater Runoff Using Sustainable Biochar: A Review, *J. Environ. Eng.*, 2023, **149**(2), 03122005, DOI: **10.1061/JOEEDU.EEENG-7049**.

53 A. I. Yunus and G. Y. Fu, Selecting the Effective Biochar for Removal of Pollutants from Highway Stormwater Runoff, *J. Environ. Eng.*, 2024, **150**(7), 04024027, DOI: **10.1061/JOEEDU.EEENG-7417**.

54 S. K. Mohanty, R. Valenca, A. W. Berger, I. K. M. Yu, X. Xiong, T. M. Saunders and D. C. W. Tsang, Plenty of Room for Carbon on the Ground: Potential Applications of Biochar for Stormwater Treatment, *Sci. Total Environ.*, 2018, 1644–1658, DOI: **10.1016/j.scitotenv.2018.01.037**.

55 A. Tomczyk, Z. Sokołowska and P. Boguta, Biochar Physicochemical Properties: Pyrolysis Temperature and Feedstock Kind Effects, *Rev. Environ. Sci. Biotechnol.*, 2020, **19**(1), 191–215, DOI: **10.1007/s11157-020-09523-3**.

56 M. Tripathi, J. N. Sahu and P. Ganesan, Effect of Process Parameters on Production of Biochar from Biomass Waste

© 2025 The Author(s). Published by the Royal Society of Chemistry

Open Access Article. Published on 18 junio 2025. Downloaded on 30/01/2026 01:29:39 p. m..
This article is licensed under a Creative Commons Attribution-NonCommercial 3.0 Unported Licence.

through Pyrolysis: A Review, *Renewable Sustainable Energy Rev.*, 2016, **55**, 467–481, DOI: **10.1016/j.rser.2015.10.122**.

57 N. Tabassam, S. Mutahir, M. A. Khan, I. U. Khan, U. Habiba and M. S. Refat, Facile Synthesis of Cinnamic Acid Sensitized Rice Husk Biochar for Removal of Organic Dyes from Wastewaters: Batch Experimental and Theoretical Studies, *Mater. Chem. Phys.*, 2022, **288**, 126327, DOI: **10.1016/j.matchemphys.2022.126327**.

58 Q. He, L. Ding, A. Raheem, Q. Guo, Y. Gong and G. Yu, Kinetics Comparison and Insight into Structure-Performance Correlation for Leached Biochar Gasification, *Chem. Eng. J.*, 2021, **417**, 129331, DOI: **10.1016/j.cej.2021.129331**.

59 A. A. Nassar, M. F. Mubarak, A. K. El-Sawaf, M. A. Zayed and M. Hemdan, Efficient Lead Ion Removal from Aqueous Solutions for Wastewater Treatment Using a Novel Cross-Linked Alginate-Rice Husk Ash-Graphene Oxide-Chitosan Nanocomposite, *Int. J. Biol. Macromol.*, 2025, **284**, 137983, DOI: **10.1016/j.ijbiomac.2024.137983**.

60 S. Ghosh, *Optimization of Phosphorus Recovery from Anaerobic Digester Supernatant through a Struvite Crystallization Fluidized Bed Reactor*, University of British Columbia, 2016, DOI: **10.14288/1.0340473**.

61 S. T. Geneti, G. A. Mekonnen, H. C. A. Murthy, E. T. Mohammed, C. R. Ravikumar, B. A. Gonfa and F. K. Sabir, Biogenic Synthesis of Magnetite Nanoparticles Using Leaf Extract of *Thymus schimperi* and Their Application for Monocomponent Removal of Chromium and Mercury Ions from Aqueous Solution, *J. Nanomater.*, 2022, **2022**(1), 5798824, DOI: **10.1155/2022/5798824**.

62 Y. Mao, J. Liu, Q. Lin, M. M. S. Abdullah, J. Wang and H. Huang, Efficient Removal of Cr(VI) and Bisphenol A by a Tannic Acid-Functionalized Porous Biochar, *Mater. Chem. Phys.*, 2024, **326**, 129770, DOI: **10.1016/j.matchemphys.2024.129770**.

63 M. Mariana, E. M. Mistar and T. Alfatah, Functional Properties and Continuous Adsorption Process of *Arenga pinnata* Shell and Its Porous Biochars for Aqueous Methylene Blue Removal, *Mater. Chem. Phys.*, 2024, **322**, 129484, DOI: **10.1016/j.matchemphys.2024.129484**.